The Influence of the Exact Evaluation of Radiation Fields in Finite Precision Arithmetic on the Stability of the Time Domain Integral Equation Method

Elwin van 't Wout, Duncan R. van der Heul, Harmen van der Ven, and Cornelis Vuik

***Abstract*—Transient electromagnetic scattering phenomena can effectively be simulated with time domain integral equation methods. The stability and accuracy of the marching on in time scheme is usually established with exact evaluation of the radiation fields. Due to singularities in their analytical expressions, straightforward evaluation in finite precision arithmetic can jeopardize the accuracy of the radiation fields. Computational experiments confirm this and show that it can even lead to late-time instability of the numerical model. Hence, a reformulation is necessary to remove the singular behavior and obtain the robustness required for industrial application. To this end, highly accurate and well-behaved expressions for the quasi-exact integration method in finite precision arithmetic will be derived in this paper. Numerical experiments confirm the robustness and stability of the improved Marching on in Time scheme.**

***Index Terms*—Accuracy, electric field integral equation, robustness, stability, time domain analysis.**

I. Introduction

THE time domain integral equation (TDIE) method can be used to model transient electromagnetic scattering phenomena [1]–[3]. The formulation in time domain allows for the analysis of broadband excitation of scattering surfaces with nonlinear responses. As a boundary integral scheme, the number of spatial degrees of freedom scales favorably to volume methods. Moreover, no artificial boundary is necessary to truncate the computational domain.

The numerical discretization follows the prevailing marching on in time (MoT) scheme, which is based on collocation and is a special form of the space-time Galerkin scheme [4]. Industrial application has long been hindered by late-time instability. Many approaches have been introduced to enhance stability [5]–[13]. The most effective one seems the use of quasi-exact integration methods that compute the discretization matrices with very high accuracy [10], [12].

The Galerkin discretization in space of the boundary integral operator results in discretization matrix elements expressed as 4-D integrals over the scattering surface. Two quasi-exact methods for the evaluation of these integrals have been established for TDIE methods in electromagnetics on arbitrary 3-D objects [10], [12]. The first method uses analytical expressions of radiation fields to compute the inner two integrals exactly. The second method uses analytical expressions for the inner three integrals, leaving one integral to be evaluated by numerical quadrature.

The main purpose of quasi-exact integration is to accomplish highly accurate computations of the elements of the discretization matrices. This is necessary because computational experiences with TDIE methods in electromagnetics show that stability is very sensitive to numerical errors, such as quadrature errors.

The choice of integration method is based on a trade-off between accuracy, efficiency, and implementation effort. In this paper, exact evaluation of the radiation fields [10] will be used, because this method is in our experience necessary and sufficient to obtain stability. The analytical expressions of radiation fields can be applied to specific basis functions only, namely the customary Rao-Wilton-Glisson (RWG) spatial basis functions and the family of piecewise polynomial temporal basis functions, which include most of the commonly used basis functions [14].

This work builds upon the elegant analytical expressions for the radiation fields as function of the geometrical properties of a source triangle and an observation point, as introduced in [10]. To the best of the authors' knowledge, the evaluation of these expressions in finite precision arithmetic has not been addressed in literature. In our experience, this is a crucial element of a robust numerical scheme.

In this paper we show that the analytical expressions of [10] are ill-behaved for certain important limit cases, for example when the observation point is projected close to a vertex of the source triangle. Because of this, a straightforward formulation in finite precision arithmetic can result in large errors in the radiation fields, and basically undermines the accuracy of the exact evaluation of the radiation fields. A computational experiment confirms this and shows it can even lead to late-time instability of the MoT scheme.

Therefore, a robust formulation will be derived that will be shown to be well-behaved for all limit cases. This results in improved accuracy in finite precision arithmetic evaluation compared to the straightforward case. In fact, the same computational experiment remains stable in late-time. The novel formulation thus improves the robustness and stability of the TDIE method and is an important step towards industrial application.

Manuscript received January 24, 2013; revised May 01, 2013 and August 27, 2013; accepted August 27, 2013. Date of publication September 10, 2013; date of current version November 25, 2013.

E. van 't Wout and H. van der Ven are with the National Aerospace Laboratory NLR, Amsterdam, Netherlands (e-mail: Elwin.van.t.wout@nlr.nl).

D. R. van der Heul and C. Vuik are with the Delft Institute of Applied Mathematics, Delft University of Technology, Delft, Netherlands.

Color versions of one or more of the figures in this paper are available online at http://ieeexplore.ieee.org.

Digital Object Identifier 10.1109/TAP.2013.2281365

This paper improves the accurate evaluation of the inner 2-D integral over the source elements on the scattering surface. The integrand of the outer 2-D integral over observation elements has a higher level of continuity and standard quadrature procedures are thus more effective. Extensive numerical simulations performed by the authors do not suggest that evaluation with a higher accuracy is necessary.

This paper will proceed as follows: Section II summarizes the model equation and its discretization. The existing quasi-exact integration method will be summarized in Section III, along with a presentation of some additional details. The implications of finite precision arithmetic will by discussed in Section IV and a straightforward formulation that eliminates the singular behavior will be applied. Because this straightforward formulation adversely effects stability, a robust formulation will be derived in Section V. In Section VI, tolerance regions are constructed according to specific requirements such that all singularities are prevented in a consistent manner. The numerical experiment in Section VII confirms that while the straightforward formulation of the analytical expressions results in an unstable MoT scheme, the robust formulation is stable. The conclusions will be presented in Section VIII.

II. Model Formulation

Let us consider a perfect electric conductor (PEC) surrounded by free space. On the interface, the incident and scattered field satisfy a homogeneous Dirichlet boundary condition for the tangential component of the electric field. With the Stratton-Chu formulation, the scattered field can be expressed in terms of the electric current distribution acting on the interface. A substitution of the Stratton-Chu formulation into the interface condition results in the model equation

$$-\hat{\mathbf{n}}\times\hat{\mathbf{n}}\times\iint_{\Gamma}\left(\mu_0\frac{\ddot{\mathbf{J}}(\mathbf{r}',\tau)}{4\pi R}-\frac{1}{\epsilon_0}\nabla\frac{\nabla'\cdot\mathbf{J}(\mathbf{r}',\tau)}{4\pi R}\right)\mathrm{d}\mathbf{r}' = -\hat{\mathbf{n}}\times\hat{\mathbf{n}}\times\dot{\mathbf{E}}^i(\mathbf{r},t) \quad (1)$$

which is the differentiated electric field integral equation (EFIE) [1]. The EFIE has to be solved for the electric surface current density $\mathbf{J}(\mathbf{r},t)$ on location $\mathbf{r}$ and time t. The dot notation $\dot{\mathbf{J}}$ has been used to denote differentiation in time. The other variables are denoted as: $\mathbf{E}^i$ the incident electric field, which is zero for $t<0$; Γ the scattering surface with outward pointing unit normal $\hat{\mathbf{n}}$; $R=|\mathbf{R}|=|\mathbf{r}-\mathbf{r}'|$; $\tau=t-R/c$ the retarded time; and ∇ and ∇' the nabla operator with respect to $\mathbf{r}$ and $\mathbf{r}'$, respectively. The speed of light is given by $c=1/\sqrt{\epsilon_0\mu_0}$ with ϵ_0 and μ_0 the permittivity and permeability of free space, respectively.

The surface of the scatterer is approximated by a set of N_s connected triangular elements and in time a uniform partitioning with levels $t_k=k\Delta t$ for $k=0,1,2,\ldots,N_t$ is adopted. The electric surface current density is expanded as

$$\mathbf{J}(\mathbf{r},t)=\sum_{n=1}^{N_s}\sum_{j=0}^{N_t}J_{n,j}\mathbf{f}_n(\mathbf{r})T_j(t) \quad (2)$$

with $\mathbf{f}_n$ and T_j denoting the basis functions in space and time, resp. The numerical discretization in space is given by the Galerkin scheme with RWG functions [15], i.e.,

$$\mathbf{f}_n(\mathbf{r})=\begin{cases}\frac{\ell_n}{2|\Gamma_n^+|}(\mathbf{r}-\mathbf{r}_n^+), & \mathbf{r}\in\Gamma_n^+\\ -\frac{\ell_n}{2|\Gamma_n^-|}(\mathbf{r}-\mathbf{r}_n^-), & \mathbf{r}\in\Gamma_n^-\end{cases} \quad (3)$$

where the triangular facets Γ_n^+ and Γ_n^- share edge n of length ℓ_n, and $\mathbf{r}_n^+$ and $\mathbf{r}_n^-$ the free vertices. Collocation is performed in time, that is, the EFIE is point matched in subsequent time levels t_k. The temporal basis functions $T_j(t)=T(t-j\Delta t)$ interpolate the solution from discrete time levels in retarded time levels. The piecewise polynomials of degree ℓ, i.e.,

$$T(s)=\begin{cases}a_{0\ell}s^\ell+\ldots+a_{01}s+a_{00}, & -1<\frac{s}{\Delta t}\le 0\\ a_{1\ell}s^\ell+\ldots+a_{11}s+a_{10}, & 0<\frac{s}{\Delta t}\le 1\\ \vdots & \vdots\\ a_{\ell\ell}s^\ell+\ldots+a_{\ell 1}s+a_{\ell 0}, & \ell-1<\frac{s}{\Delta t}\le\ell\end{cases} \quad (4)$$

will be used since they include many of the popular temporal basis functions [14], including the shifted Lagrange interpolants [16]. Because the temporal basis functions are discretely causal, they satisfy the marching criterion [8]. Then, the discrete model equations can be written as the MoT scheme

$$Z_0\mathbf{j}_k=\mathbf{c}_k-\sum_{i=1}^{k}Z_i\mathbf{j}_{k-i} \quad (5)$$

where $\mathbf{j}_k$ and $\mathbf{c}_k$ denote the discrete surface current density and incident field at time t_k, resp. The discretization matrices Z_i represent the interaction of each triangle pair at each retarded time level. An arbitrary matrix element (m,n) is given by

$$(Z_i)_{mn}=\frac{1}{c}\iint_{\hat{\Gamma}}\mathbf{f}_m(\mathbf{r})\cdot\iint_{\hat{\Gamma}}\frac{\mathbf{f}_n(\mathbf{r}')\ddot{T}\left(i\Delta t-\frac{|\mathbf{r}-\mathbf{r}'|}{c}\right)}{4\pi|\mathbf{r}-\mathbf{r}'|}\mathrm{d}\mathbf{r}'\mathrm{d}\mathbf{r}$$
$$+c\iint_{\hat{\Gamma}}\nabla\cdot\mathbf{f}_m(\mathbf{r})\iint_{\hat{\Gamma}}\frac{\nabla'\cdot\mathbf{f}_n(\mathbf{r}')T\left(i\Delta t-\frac{|\mathbf{r}-\mathbf{r}'|}{c}\right)}{4\pi|\mathbf{r}-\mathbf{r}'|}\mathrm{d}\mathbf{r}'\mathrm{d}\mathbf{r} \quad (6)$$

where $\hat{\Gamma}$ denotes the surface mesh.

III. Analytical Formulation of Radiation Fields

This section describes the analytical formulation of the radiation fields and explains its incorporation in the MoT scheme. Most of the material discussed here has been introduced in [10]. This section aims to introduce the nomenclature that will be used in subsequent sections and provides additional details that will be used in the analysis of the evaluation in finite precision arithmetic.

For conciseness, only the application to the differentiated EFIE (1) will be considered in this paper, but the same algorithm can also be used for other boundary integral equations, including the MFIE, PMCHWT, and Müller equations [10].

A. Derivation of Standard Intersection Integrals

The goal of this section is to rewrite the elements of the discretization matrix (6) into a standardized form. First, the local support of the RWG function (3) is used to simplify the integration domain into pairs of observer and source triangular facets, denoted by Γ_p and Γ_q, resp. A numerical quadrature procedure will be used for the outer integral over the observer triangle.

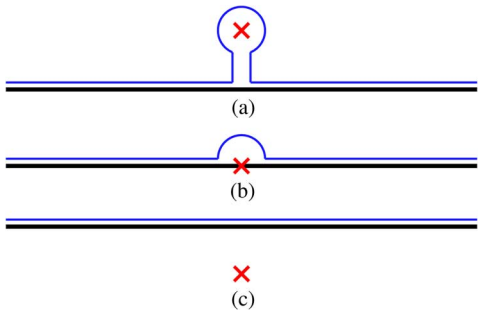

Fig. 1. Three cases of the contour integration, with the edge (black), the projection point (red cross), and the contour (blue), where the inside of the triangle is located above the edge. (a) The keyhole contour for a pole inside the triangle. (b) The indented contour for a pole on the edge. (c) The line contour for a pole outside the triangle.

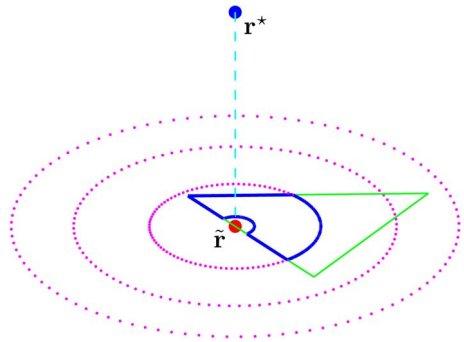

Fig. 2. Contour of an intersection of a triangle and discrete light cone. Depicted are the triangle (green), observer point (blue point), projection (cyan dotted line), projection point (red point), discrete light cones on the projection plane (magenta dotted line) and contour (blue).

Then, the radiation fields are expressed by an integral operator with respect to an *observer point*, denoted by $\mathbf{r}^\star$. The expressions can be simplified by considering the *projection point*, denoted by $\tilde{\mathbf{r}}$ and defined as the orthogonal projection of $\mathbf{r}^\star$ onto the plane through source triangle Γ_q. This introduces the *projection height*, denoted by $h = |\tilde{\mathbf{r}} - \mathbf{r}^\star|$.

The temporal basis functions (4) are defined as piecewise polynomials. To obtain a single expression for the radiation field, the integration over the source triangle Γ_q should be partitioned into regions where the temporal basis functions are uniquely defined. This is the case for all source points $\mathbf{r}'$ satisfying $j \leq |\mathbf{r}^\star - \mathbf{r}'|/(c\Delta t) < j+1$ for an integer j. This represents the discrete light cone of observer point $\mathbf{r}^\star$ with interval Δt. The integration should thus be reduced to

$$\Gamma_{q,j} = \left\{ \mathbf{r}' \in \Gamma_q \mid j\Delta t \leq \frac{|\mathbf{r}^\star - \mathbf{r}'|}{c} < (j+1)\Delta t \right\} \tag{7}$$

which is the intersection of the source triangle and the discrete light cone.

Now, each element of the discretization matrix can be written as a unique combination of *standard intersection integrals*, given by

$$\mathbf{I}_k(\mathbf{r}^\star) = \iint_{\Gamma_{q,j}} (\mathbf{r}' - \tilde{\mathbf{r}}) |\mathbf{r}^\star - \mathbf{r}'|^k \mathrm{d}\mathbf{r}', \tag{8a}$$

$$I_k(\mathbf{r}^\star) = \iint_{\Gamma_{q,j}} |\mathbf{r}^\star - \mathbf{r}'|^k \mathrm{d}\mathbf{r}' \tag{8b}$$

for $k = -3, -1, 0, 1, \ldots, \ell - 1$.

B. Derivation of Standard Contour Integrals

Using Gauss' theorem, surface integrals can be rewritten into contour integrals. The standard intersection integrals (8) can thus be simplified as the *standard contour integrals*

$$\mathbf{I}_k(\mathbf{r}^\star) = \frac{1}{k+2} \oint_{\partial\Gamma_{q,j}} |\mathbf{r}^\star - \mathbf{r}'|^{k+2} \hat{\mathbf{d}} \mathrm{d}\mathbf{r}', \tag{9a}$$

$$I_k(\mathbf{r}^\star) = \frac{1}{k+2} \oint_{\partial\Gamma_{q,j}} \frac{|\mathbf{r}^\star - \mathbf{r}'|^{k+2}}{|\mathbf{r}' - \tilde{\mathbf{r}}|^2} (\mathbf{r}' - \tilde{\mathbf{r}}) \cdot \hat{\mathbf{d}} \mathrm{d}\mathbf{r}' \tag{9b}$$

for $k = -3, -1, 0, 1, \ldots, \ell - 1$, where $\hat{\mathbf{d}}$ denotes the unit outward normal on $\partial\Gamma_{q,j}$ situated inside the plane through the triangle. Special care should be devoted to the definition of the contour $\partial\Gamma_{q,j}$. The integrand of the scalar contour integrals (9b) contains a singularity at $\mathbf{r}' = \tilde{\mathbf{r}}$, which occurs when the observer point is projected onto the source triangle. This is an integrable singularity, so the integral operators converge and the singular point is called a *pole*. Hence, the inside of contour $\partial\Gamma_{q,j}$ should exclude the pole, which can be done with a keyhole or indented contour, see Fig. 1. Then, a limit process will be performed such that the contour converges to the boundary of $\Gamma_{q,j}$. However, nonzero limit values of the standard contour integrals can be obtained at the pole, which will be denoted by I_k^{pole} for $k = -3, -1, 0, 1, \ldots, \ell - 1$, called the *standard pole integrals*.

Remember that $\Gamma_{q,j}$ is given by the intersection of a triangle and a discrete light cone. Therefore, the contour $\partial\Gamma_{q,j}$ consists of line segments and arcs only, see Fig. 2. The standard contour integrals can thus be written as a unique combination of standard line, arc, and pole integrals:

$$\mathbf{I}_k(\mathbf{r}^\star) = \sum_{i=1}^{\#\text{line segments}} \mathbf{I}_k^{\mathrm{line},i}(\mathbf{r}^\star) + \sum_{i=1}^{\#\text{arcs}} \mathbf{I}_k^{\mathrm{arc},i}(\mathbf{r}^\star), \tag{10a}$$

$$I_k(\mathbf{r}^\star) = \sum_{i=1}^{\#\text{line segments}} I_k^{\mathrm{line},i}(\mathbf{r}^\star) + \sum_{i=1}^{\#\text{arcs}} I_k^{\mathrm{arc},i}(\mathbf{r}^\star) + I_k^{\mathrm{pole}}(\mathbf{r}^\star) \tag{10b}$$

where the number of line segments and arcs depend on the intersection shape. These numbers range from zero to three. An analytical expression for the standard contour integrals can be derived separately for each line segment and arc.

C. Analytical Expression for Standard Line Integrals

Let us consider an arbitrary line segment that is part of the contour and denote its start and end point by $\mathbf{r}_1$ and $\mathbf{r}_2$, resp. In order to derive an analytical expression of the standard contour integrals (9) on a line segment, let us introduce the local coordinate system $(\hat{\mathbf{u}}, \hat{\mathbf{v}}, \hat{\mathbf{w}})$ defined by

$$\hat{\mathbf{u}} = \frac{(\mathbf{r}_2 - \mathbf{r}_1)}{|\mathbf{r}_2 - \mathbf{r}_1|} \tag{11a}$$

$$\hat{\mathbf{v}} = \hat{\mathbf{u}} \times \hat{\mathbf{w}} \tag{11b}$$

$$\hat{\mathbf{w}} = \hat{\mathbf{n}} \tag{11c}$$

where $\hat{\mathbf{n}}$ denotes the unit outward normal on the surface mesh. The vectors $\hat{\mathbf{u}}$ and $\hat{\mathbf{v}}$ are situated in the plane of the triangular mesh element and are oriented parallel and perpendicular to the

line segment, resp. The location of the projection point $\tilde{\mathbf{r}}$ w.r.t. this line segment can be characterized by the parameters

$$u_1 = (\mathbf{r}_1 - \tilde{\mathbf{r}}) \cdot \hat{\mathbf{u}} \tag{12a}$$
$$u_2 = (\mathbf{r}_2 - \tilde{\mathbf{r}}) \cdot \hat{\mathbf{u}} \tag{12b}$$
$$v_0 = (\mathbf{r}_1 - \tilde{\mathbf{r}}) \cdot \hat{\mathbf{v}} \tag{12c}$$
$$w_0 = |(\mathbf{r}_1 - \tilde{\mathbf{r}}) \cdot \hat{\mathbf{w}}| = h. \tag{12d}$$

The analytical expression of the *vector line integrals* from (10) is given by

$$\mathbf{I}_k^{\text{line}}(\mathbf{r}^\star) = \frac{L_k^{\text{vector}}}{k+2}\hat{\mathbf{v}} \tag{13}$$

for $k = -3, -1, 0, 1, \ldots, \ell - 1$, with

$$L_{-3}^{\text{vector}} = \ln\left(\frac{u_2 + |\mathbf{r}_2 - \mathbf{r}^\star|}{u_1 + |\mathbf{r}_1 - \mathbf{r}^\star|}\right) \tag{14a}$$

$$L_0^{\text{vector}} = \frac{1}{2}|\mathbf{r}_2 - \mathbf{r}_1|\left(|\mathbf{r}_2 - \mathbf{r}^\star|^2 + |\mathbf{r}_1 - \mathbf{r}^\star|^2 - \frac{1}{3}|\mathbf{r}_2 - \mathbf{r}_1|^2\right) \tag{14b}$$

$$L_k^{\text{vector}} = \frac{1}{k+3}\left(u_2|\mathbf{r}_2 - \mathbf{r}^\star|^{k+2} - u_1|\mathbf{r}_1 - \mathbf{r}^\star|^{k+2}\right) + \frac{k+2}{k+3}(v_0 + h^2)L_{k-2}^{\text{vector}} \tag{14c}$$

for $k = -1, 1, 2, 3, \ldots, \ell - 1$. The analytical expression of the *scalar line integrals* is given by

$$I_{-3}^{\text{line}}(\mathbf{r}^\star) = \begin{cases} -\frac{1}{h}\left(\arctan\left(\frac{u_2}{v_0}\frac{h}{|\mathbf{r}_2 - \mathbf{r}^\star|}\right) - \arctan\left(\frac{u_1}{v_0}\frac{h}{|\mathbf{r}_1 - \mathbf{r}^\star|}\right)\right), & v_0 \neq 0 \text{ and } h \neq 0 \\ 0, & v_0 = 0 \text{ or } h = 0 \end{cases} \tag{15a}$$

$$I_0^{\text{line}}(\mathbf{r}^\star) = \begin{cases} \frac{1}{2}h^2\left(\arctan\left(\frac{u_2}{v_0}\right) - \arctan\left(\frac{u_1}{v_0}\right)\right) + \frac{1}{2}v_0|\mathbf{r}_2 - \mathbf{r}_1|, & v_0 \neq 0 \\ 0, & v_0 = 0 \end{cases} \tag{15b}$$

$$I_k^{\text{line}}(\mathbf{r}^\star) = \frac{v_0}{k+2}L_{k-2}^{\text{vector}} + \frac{k}{k+2}h^2 I_{k-2}^{\text{line}}(\mathbf{r}^\star) \tag{15c}$$

for $k = -1, 1, 2, 3, \ldots, \ell - 1$. Notice that the scalar line integrals are given by a recurrence relation (15c) which requires both an odd and even initial term, given by (15a) and (15b) for -3 and 0, resp.

D. Analytical Expression for Standard Arc Integrals

Let us consider an arbitrary arc that is part of the contour and denote its start and end point by $\mathbf{r}_1$ and $\mathbf{r}_2$, resp. The analytical expression of the standard contour integrals (9) on an arc is given by

$$\mathbf{I}_k^{\text{arc}}(\mathbf{r}^\star) = \frac{(\mathbf{r}_2 - \mathbf{r}_1) \times \hat{\mathbf{n}}}{k+2}|\mathbf{r}_1 - \mathbf{r}^\star|^{k+2} \tag{16a}$$

$$I_k^{\text{arc}}(\mathbf{r}^\star) = \frac{\theta}{k+2}|\mathbf{r}_1 - \mathbf{r}^\star|^{k+2} \tag{16b}$$

for $k = -3, -1, 0, 1, \ldots, \ell - 1$, where θ denotes the angle of the arc.

E. Analytical Expression for Standard Pole Integrals

The scalar standard contour integrals (10b) contain pole integrals, with the analytical expression given by

$$I_k^{\text{pole}}(\mathbf{r}^\star) = -\varphi(\tilde{\mathbf{r}})\frac{h^{k+2}}{k+2} \tag{17}$$

for $k = -3, -1, 0, 1, \ldots, \ell - 1$, where φ denotes the circumscribed angle, given by

$$\varphi(\mathbf{r}) = \begin{cases} 2\pi, & \mathbf{r} \text{ inside triangle} \\ \pi, & \mathbf{r} \text{ on edge} \\ \alpha_i, & \mathbf{r} \text{ on vertex } i \\ 0, & \mathbf{r} \text{ outside triangle} \end{cases} \tag{18}$$

where $0 < \alpha_i < \pi$ denotes the inner angle of the two edges connecting to vertex i. Notice that the standard pole integrals (17) can be written as the recurrence relation

$$I_k^{\text{pole}}(\mathbf{r}^\star) = \frac{k}{k+2}h^2 I_{k-2}^{\text{pole}}(\mathbf{r}^\star) \tag{19}$$

for $k = -1, 1, 2, 3, \ldots, \ell - 1$.

IV. Finite Precision Arithmetic

In this section, a thorough analysis of the consequences of analytic evaluation of the contour integrals (9) in finite precision arithmetic will be derived. It will be shown that the analytical expressions of the radiation fields suffer from singular behavior when the projection of the observation point approaches the boundary of the source element. A straightforward evaluation in finite precision arithmetic will be given.

A. Straightforward Evaluation in Finite Precision Arithmetic

The required formulation of the analytical expressions of the radiation fields in finite precision arithmetic can best be explained for the standard pole integrals (17), which depends on the circumscribed angle (18). The piecewise definition of the circumscribed angle makes it necessary to establish the location of the projection point w.r.t. the triangular facet. For instance, one has to check if a projection point $\tilde{\mathbf{r}}$ coincides with a vertex $\mathbf{v}_i$. Due to rounding errors, the check $|\tilde{\mathbf{r}} - \mathbf{v}_i| = 0$ is not meaningful in finite precision arithmetic. Instead, one has to use $\|\mathbf{r} - \mathbf{v}_i\| < \epsilon$ for $\epsilon > 0$ small compared to a characteristic length scale of the surface mesh elements. Hence, when the projection point is located in the *tolerance region* $\{\mathbf{r} \in \mathbb{R}^3, \|\mathbf{r} - \mathbf{v}_i\| < \epsilon\}$ around the vertex, they will be considered as if they coincide. The standard pole integrals are then given by

$$\hat{I}_k^{\text{pole}}(\mathbf{r}^\star) = -\hat{\varphi}(\tilde{\mathbf{r}})\frac{h^{k+2}}{k+2} \tag{20a}$$

$$\hat{\varphi}(\mathbf{r}) = \begin{cases} 2\pi, & \mathbf{r} \text{ inside triangle and outside tol. regions} \\ \pi, & \mathbf{r} \text{ inside edge tolerance regions} \\ \alpha_i, & \mathbf{r} \text{ inside tolerance region of vertex } i \\ 0, & \mathbf{r} \text{ outside triangle and tolerance regions} \end{cases} \tag{20b}$$

for finite precision arithmetic. The full definition of the different tolerance regions will be given in Section VI.

Similarly, the scalar line integrals (15) are piecewise defined for $v_0 = 0$ and $v_0 \neq 0$. Geometrically, this corresponds to pro-

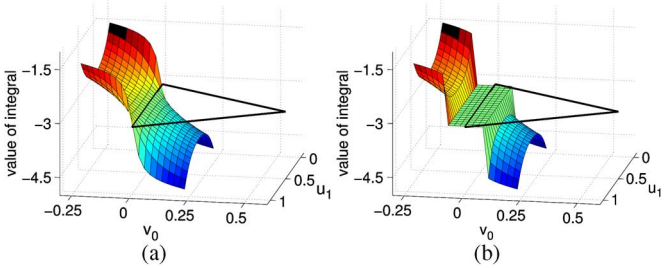

Fig. 3. Value of $I_0^{\text{line}} + I_0^{\text{pole}}$ w.r.t. projection points $\tilde{\mathbf{r}}$ close to an edge. Horizontal axes denote the local coordinates $(\hat{\mathbf{u}}, \hat{\mathbf{v}})$ from (11). The vertical axis and colors in the surface plot depict the value of the integral. The shape of the source triangle is depicted by the black lines. (a) The analytical expression, given by (15) and (17). (b) The straightforward formulation for finite precision arithmetic, given by (21) and (20), with $|v_0| < 0.1$ as tolerance region.

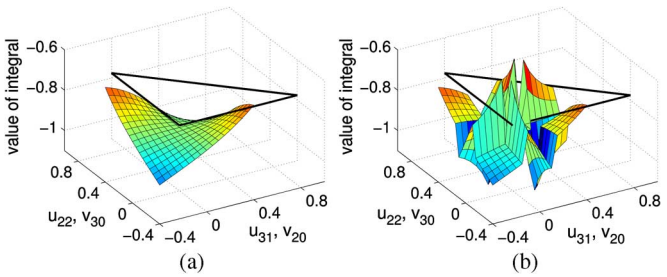

Fig. 4. Value of $I_0^{\text{line},2} + I_0^{\text{line},3} + I_0^{\text{pole}}$ w.r.t. projection points $\tilde{\mathbf{r}}$ close to vertex 1. Horizontal axes denote the local coordinates $(\hat{\mathbf{u}}, \hat{\mathbf{v}})$ from (11). The vertical axis and colors in the surface plot depict the value of the integral. The shape of the source triangle is depicted by the black lines. (a) The analytical expression, given by (15) and (17). (b) The straightforward formulation for finite precision arithmetic, given by (21) and (20), with $|v_0| < 0.1$ as tolerance region.

jection on or outside an edge, resp. For finite precision arithmetic, a tolerance region around the edge will be necessary and the scalar line integrals are extended into

$$\hat{I}_k^{\text{line}}(\mathbf{r}^\star) = \begin{cases} \frac{v_0}{k+2} L_{k-2}^{\text{vector}} \\ \quad + \frac{k}{k+2} h^2 \hat{I}_{k-2}^{\text{line}}(\mathbf{r}^\star), & \tilde{\mathbf{r}} \text{ outside tolerance region} \\ 0, & \tilde{\mathbf{r}} \text{ inside tolerance region} \end{cases} \tag{21}$$

for $k = -1, 1, 2, 3, \ldots, \ell - 1$, where the initial values $\hat{I}_{-3}^{\text{line}}$ and $\hat{I}_0^{\text{line}}$ are given by (15). The analytical expression of a standard contour integral and its extended expression for finite precision arithmetic are depicted in Figs. 3 and 4. For presentation, an extremely large tolerance region has been used.

Fig. 3 depicts the case where the projection point is located close to an edge. A constant approximation has been used inside the edge tolerance region, which results in a discontinuity at the boundary of the tolerance region.

When the observer point is projected close to a vertex, both a vertex tolerance region and an edge tolerance region for the adjacent edges are necessary. As depicted in Fig. 4, numerical errors are present in the straightforward formulation whereas the analytical expression of the contour integral is smooth. It will be shown in Section V that different terms in the analytical expression cancel out on the edges of the triangular facets. Because of the constant approximations inside the tolerance regions, this cancellation is not effective anymore, which causes inaccurate expressions for the standard contour integrals.

B. Requirements on Robust Formulations

In Section IV-A, an extended version of the analytical expressions of radiation fields has been introduced, which is necessary for finite precision arithmetic. This straightforward formulation results in discontinuous and inaccurate expressions for the standard contour integrals. Although these inaccuracies might be small for each radiation field, they could accumulate into inaccurate discretization matrix elements and ultimately in an unstable MoT scheme, as will be experimentally confirmed in Section VII.

This paper aims to derive a robust formulation for the quasi-exact integration method where all analytical expressions of radiation fields are well-behaved and hence eliminates this specific cause of instability. *Well-behaved* will be defined as

1) accurate, and
2) nonsingular.

The accuracy is defined as the difference between the formulation for finite precision arithmetic and the analytical expression of the standard contour integrals. Outside the tolerance regions, the analytical expressions from Section III are used, which introduce no errors, apart from rounding errors. However, an approximation will be used inside the tolerance regions. In the straightforward formulation, a constant approximation has been used. In the next section, a robust formulation will be derived that is highly accurate. In fact, for most cases the novel formulation will be equivalent to the analytical expression.

The main reason for the necessity to use tolerance regions in the analytical expression is the singular dependence on the location of the observer point. That is, some terms in the exact formulation contain a division by a parameter that can be arbitrarily small. Although these singularities might be properly defined for exact arithmetic, for finite precision arithmetic these singularities could cause excessive rounding errors. To this end, a division by a parameter in the robust formulation is only allowed when the absolute value of the parameter has a strictly positive lower bound.

V. Robust Formulation of Analytical Expressions

In Section IV-A a straightforward formulation has been introduced for the analytical expressions of the radiation fields when finite precision arithmetic is used. Because this straightforward formulation contains expressions that are not well-behaved, a robust formulation will be derived in this section.

It can be shown that the scalar line (15) and pole integrals (17) are the only parts of the standard contour integrals (10) that are not well-behaved, according to the requirements in Section IV-B. The deficiencies occur near the boundary of each triangular element and the novel expressions will, therefore, be used inside the tolerance regions only. Due to cancellation of some terms in their respective analytical expressions, one can only achieve well-behaved expressions when the sum of the contribution of the scalar line and pole integrals is considered, as opposed to considering these separately.

The expressions in the robust formulation are well-behaved, even for finite precision arithmetic. That is, the radiation fields are represented very accurate and the singular behavior of the original formulation is completely eliminated.

A. Robust Formulation Near an Edge

First, a robust formulation will be derived for projection points close to an edge of the source triangle, but sufficiently far

away from the vertices. The scalar line integrals (15) contain terms in the form of $\arctan(C/v_0)$ with a constant $C > 0$. The parameter v_0, given by (12c), represents the distance from the projection point to the edge and can, therefore, become arbitrary small. However, the limit

$$\lim_{v_0 \to 0} \arctan\left(\frac{C}{v_0}\right) = \begin{cases} \frac{\pi}{2}, & v_0 > 0 \\ -\frac{\pi}{2}, & v_0 < 0 \end{cases} \tag{22}$$

converges, where $v_0 > 0$ and $v_0 < 0$ correspond to a projection point inside or outside the source triangle, resp. This singularity can be rewritten with the calculus identity

$$\arctan\left(\frac{x}{y}\right) = \begin{cases} \frac{\pi}{2} - \arctan\left(\frac{y}{x}\right), & xy > 0 \\ -\frac{\pi}{2} - \arctan\left(\frac{y}{x}\right), & xy < 0 \end{cases} \tag{23}$$

for arbitrary nonzero x and y.

Because the scalar line and pole integrals satisfy the recurrence relations (15c) and (19), it suffices to rewrite the scalar line and pole integrals for $k = -3$ and $k = 0$ only. With the use of (23), the sum of the scalar line and pole integrals can be rewritten as

$$\begin{aligned} &- h\left(I_{-3}^{\text{line}}(\mathbf{r}^\star) + I_{-3}^{\text{pole}}(\mathbf{r}^\star)\right) \\ &= \begin{cases} \arctan\left(\frac{u_2}{v_0}\frac{h}{|\mathbf{r}_2-\mathbf{r}^\star|}\right) \\ \quad - \arctan\left(\frac{u_1}{v_0}\frac{h}{|\mathbf{r}_1-\mathbf{r}^\star|}\right) - 2\pi, & v_0 > 0 \\ 0 - \pi, & v_0 = 0 \\ \arctan\left(\frac{u_2}{v_0}\frac{h}{|\mathbf{r}_2-\mathbf{r}^\star|}\right) \\ \quad - \arctan\left(\frac{u_1}{v_0}\frac{h}{|\mathbf{r}_1-\mathbf{r}^\star|}\right) - 0, & v_0 < 0 \end{cases} \\ &= \begin{cases} \frac{\pi}{2} - \arctan\left(\frac{v_0}{u_2}\frac{|\mathbf{r}_2-\mathbf{r}^\star|}{h}\right) \\ \quad + \frac{\pi}{2} + \arctan\left(\frac{v_0}{u_1}\frac{|\mathbf{r}_1-\mathbf{r}^\star|}{h}\right) - 2\pi, & v_0 > 0 \\ -\pi, & v_0 = 0 \\ \frac{\pi}{2} - \arctan\left(\frac{v_0}{u_2}\frac{|\mathbf{r}_2-\mathbf{r}^\star|}{h}\right) \\ \quad + \frac{\pi}{2} + \arctan\left(\frac{v_0}{u_1}\frac{|\mathbf{r}_1-\mathbf{r}^\star|}{h}\right), & v_0 < 0 \end{cases} \\ &= \arctan\left(\frac{v_0}{u_1}\frac{|\mathbf{r}_1-\mathbf{r}^\star|}{h}\right) - \arctan\left(\frac{v_0}{u_2}\frac{|\mathbf{r}_2-\mathbf{r}^\star|}{h}\right) - \pi \end{aligned} \tag{24a}$$

$$\begin{aligned} &\frac{2}{h^2}\left(I_0^{\text{line}}(\mathbf{r}^\star) + I_0^{\text{pole}}(\mathbf{r}^\star)\right) \\ &= \begin{cases} v_0\frac{|\mathbf{r}_2-\mathbf{r}_1|}{h^2} + \arctan\left(\frac{u_2}{v_0}\right) \\ \quad - \arctan\left(\frac{u_1}{v_0}\right) - 2\pi, & v_0 > 0 \\ 0 - \pi, & v_0 = 0 \\ v_0\frac{|\mathbf{r}_2-\mathbf{r}_1|}{h^2} + \arctan\left(\frac{u_2}{v_0}\right) \\ \quad - \arctan\left(\frac{u_1}{v_0}\right) - 0, & v_0 < 0 \end{cases} \\ &= \begin{cases} v_0\frac{|\mathbf{r}_2-\mathbf{r}_1|}{h^2} + \frac{\pi}{2} - \arctan\left(\frac{v_0}{u_2}\right) \\ \quad + \frac{\pi}{2} + \arctan\left(\frac{v_0}{u_1}\right) - 2\pi, & v_0 > 0 \\ -\pi, & v_0 = 0 \\ v_0\frac{|\mathbf{r}_2-\mathbf{r}_1|}{h^2} + \frac{\pi}{2} - \arctan\left(\frac{v_0}{u_2}\right) \\ \quad + \frac{\pi}{2} + \arctan\left(\frac{v_0}{u_1}\right), & v_0 < 0 \end{cases} \\ &= v_0\frac{|\mathbf{r}_2-\mathbf{r}_1|}{h^2} + \arctan\left(\frac{v_0}{u_1}\right) - \arctan\left(\frac{v_0}{u_2}\right) - \pi. \end{aligned} \tag{24b}$$

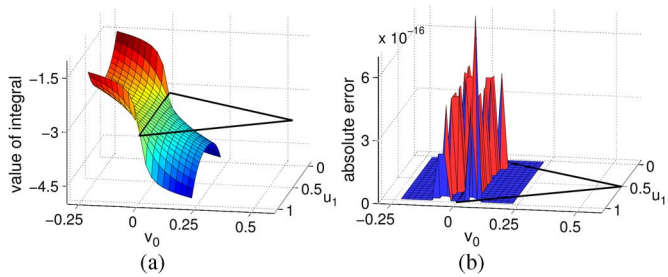

Fig. 5. Value of $I_0^{\text{line}} + I_0^{\text{pole}}$ w.r.t. projection points $\tilde{\mathbf{r}}$ close to an edge. Horizontal axes denote the local coordinates $(\hat{\mathbf{u}}, \hat{\mathbf{v}})$ from (11). The vertical axis and colors in the surface plot depict the value of the integral. The shape of the source triangle is depicted by the black lines. (a) The robust formulation, given by (24), with edge tolerance region $|v_0| < 0.1$. (b) The absolute difference between the robust formulation and analytical expression.

This novel formulation is depicted in Fig. 5. Because an exact reformulation has been derived, no errors are introduced except of rounding errors. This is in contrast to the straightforward formulation, as can be clearly seen with a comparison with Fig. 3(b), where the same tolerance region has been used.

Important to notice is that because of the use of identity (23) the singularities are shifted from small v_0 to small u_1 and u_2. Geometrically, the singularity has been replaced from the edge to the vertices. Therefore, vertices have to be excluded from the edge tolerance regions. This will be a requirement for the definition of the tolerance regions, see Section VI.

B. Robust Formulation Near the Extension of an Edge

The singularity for small v_0 in the scalar line integrals (15) occurs not only for projection near an edge, also for projection near the extension of an edge. Therefore, a novel formulation has to be derived for projection points close to the rays that extend the edges. This *ray tolerance region* is depicted in yellow in Fig. 9. Because the ray tolerance region is always outside the source triangle, the standard pole integrals (17) are zero and only the scalar line integrals have to be rewritten. Similar to (24), the scalar line integrals can be expressed as

$$I_{-3}^{\text{line}}(\mathbf{r}^\star) = \frac{1}{h}\arctan\left(\frac{v_0}{u_2}\frac{|\mathbf{r}_2-\mathbf{r}^\star|}{h}\right) - \frac{1}{h}\arctan\left(\frac{v_0}{u_1}\frac{|\mathbf{r}_1-\mathbf{r}^\star|}{h}\right) \tag{25a}$$

$$I_0^{\text{line}}(\mathbf{r}^\star) = \frac{v_0}{2}|\mathbf{r}_2-\mathbf{r}_1| + \frac{h^2}{2}\left(\arctan\left(\frac{v_0}{u_1}\right) - \arctan\left(\frac{v_0}{u_2}\right)\right) \tag{25b}$$

inside the ray tolerance regions.

C. Robust Formulation Near a Vertex

For projection near a vertex, three parts of the standard contour integrals (10) have to be rewritten to enable a robust formulation. These are the scalar line integrals (15) on the two adjacent edges and the standard pole integrals (17). To this end, let us consider a projection point $\tilde{\mathbf{r}}$ close to vertex 1, with edges 2 and 3 adjacent, as depicted in Fig. 6. The line integrals run from $\mathbf{r}_2$ to $\mathbf{v}_1$ and from $\mathbf{v}_1$ to $\mathbf{r}_3$ over edge 2 and 3, resp. Two sets of local coordinates (11) and parameters (12) have to be used, namely $(\hat{\mathbf{u}}_2, \hat{\mathbf{v}}_2, \hat{\mathbf{w}}_2), (u_{21}, u_{22}, v_{20}, w_0)$ for edge 2 and $(\hat{\mathbf{u}}_3, \hat{\mathbf{v}}_3, \hat{\mathbf{w}}_3), (u_{31}, u_{32}, v_{30}, w_0)$ for edge 3.

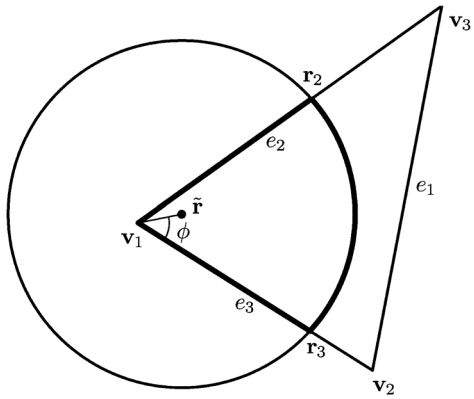

Fig. 6. Arbitrary projection point $\tilde{\mathbf{r}}$ and triangle with vertices $(\mathbf{v}_1, \mathbf{v}_2, \mathbf{v}_3)$ and edges (e_1, e_2, e_3). The contour is given by two line segments and one arc passing through points $(\mathbf{r}_2, \mathbf{v}_1, \mathbf{r}_3)$. The angle of the projection point w.r.t. vertex 1 is denoted by ϕ.

If the projection point is located on vertex 1, all parameters u_{22}, u_{31}, v_{20}, and v_{30} are zero. But parameters $u_{21} < 0$ and $u_{32} > 0$ have a lower bound, which allows for the use of

$$\arctan\left(\frac{u_{21}}{v_{20}}\right) = -\frac{\pi}{2} - \arctan\left(\frac{v_{20}}{u_{21}}\right) \tag{26a}$$

$$\arctan\left(\frac{u_{32}}{v_{30}}\right) = \frac{\pi}{2} - \arctan\left(\frac{v_{30}}{u_{32}}\right) \tag{26b}$$

equivalent to calculus identity (23). By geometrical identities,

$$\arctan\left(\frac{u_{22}}{v_{20}}\right) = \begin{cases} \phi - \alpha_1 - \frac{\pi}{2}, & -\pi < \alpha_1 - \phi < 0 \\ \phi - \alpha_1 + \frac{\pi}{2}, & 0 < \alpha_1 - \phi < \pi \end{cases} \tag{27a}$$

$$\arctan\left(\frac{u_{31}}{v_{30}}\right) = \begin{cases} \phi + \frac{\pi}{2}, & -\pi < \phi < 0 \\ \phi - \frac{\pi}{2}, & 0 < \phi < \pi \end{cases} \tag{27b}$$

where α_1 denotes the angle of vertex 1 and ϕ the angle from edge 3 to the projection point, as depicted in Fig. 6. The identities (26) and (27) are sufficient to derive a well-behaved expression for the standard contour integral I_0. The derivation is given by (29b), shown at the bottom of the (next) page. Notice that in this derivation, only three location cases of the projection point w.r.t. the vertex have been given, whereas the derivation for the other cases is similar.

The standard contour integral I_{-3} cannot be rewritten exactly into a well-behaved expression, because the geometrical identities (27) are not valid. Instead, one can combine it with the approximations

$$\arctan\left(\frac{u_{22}}{v_{20}}\frac{h}{|\mathbf{v}_1 - \mathbf{r}^\star|}\right) = \arctan\left(\frac{u_{22}}{v_{20}}\right) + \mathcal{O}\left(|v_{20}|^2\right) \tag{28a}$$

$$\arctan\left(\frac{u_{31}}{v_{30}}\frac{h}{|\mathbf{v}_1 - \mathbf{r}^\star|}\right) = \arctan\left(\frac{u_{31}}{v_{30}}\right) + \mathcal{O}\left(|v_{30}|^2\right) \tag{28b}$$

that have been derived with a Taylor series. Notice that when $|v_0| < \epsilon$ holds inside the tolerance region, the truncation error is $\mathcal{O}(\epsilon^2)$. The derivation of I_{-3} is given in (29a), shown at the bottom of the (next) page. Remember that for larger k the recurrence relations (15c) and (19) can be used [see (29a) and (29b) at the bottom of the next page].

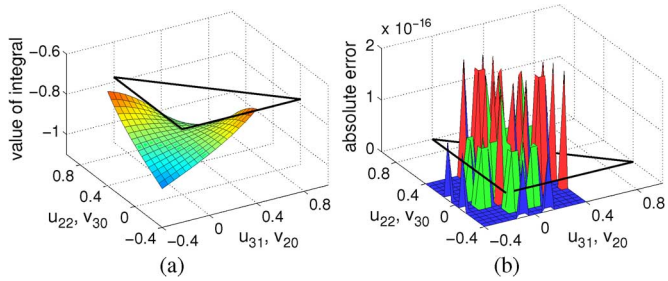

Fig. 7. Value of $I_0^{\text{line},2} + I_0^{\text{line},3} + I_0^{\text{pole}}$ w.r.t. projection points $\tilde{\mathbf{r}}$ close to vertex 1. Horizontal axes denote the local coordinates $(\hat{\mathbf{u}}, \hat{\mathbf{v}})$ from (11). The vertical axis and colors in the surface plot depict the value of the integral. The shape of the source triangle is depicted by the black lines. (a) The robust formulation, given by (29) and (24), with $|v_0| < 0.1$ as tolerance region. (b) The absolute difference between the robust formulation and analytical expression.

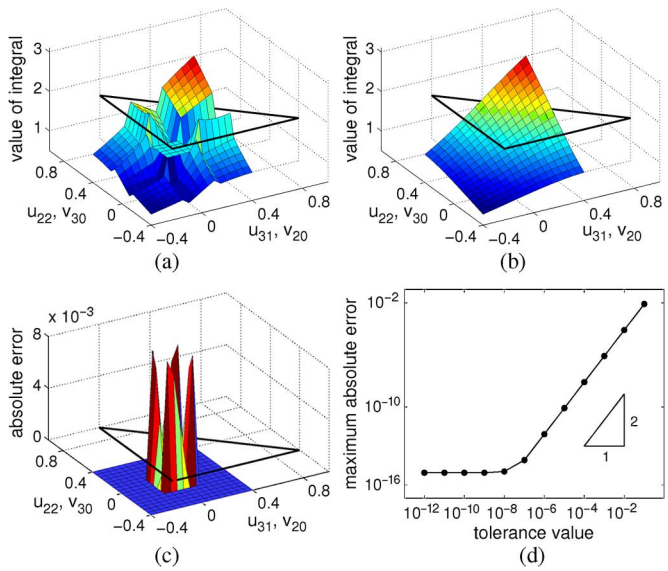

Fig. 8. Value of $I_{-3}^{\text{line},2} + I_{-3}^{\text{line},3} + I_{-3}^{\text{pole}}$ w.r.t. projection points $\tilde{\mathbf{r}}$ close to vertex 1. Horizontal axes denote the local coordinates $(\hat{\mathbf{u}}, \hat{\mathbf{v}})$ from (11). The vertical axis and colors in the surface plot depict the value of the integral. The shape of the source triangle is depicted by the black lines. (a) The straightforward formulation, given by (21) and (20), with $|v_0| < 0.1$ as tolerance region. (b) The robust formulation, given by (29) and (24), with $|v_0| < 0.1$ as tolerance region. (c) The absolute difference between the robust formulation and analytical expression. (d) The convergence of the error in the robust formulation w.r.t. the tolerance value.

The standard contour integral I_0 computed with the robust formulation is depicted in Fig. 7(a). A comparison with the straightforward formulation, depicted in Fig. 4(b) with the same tolerance regions, shows that the robust formulation improves the accuracy tremendously. The error is approximately 10^{-16}, as depicted in Fig. 7(b), which confirms that only rounding errors are present.

Fig. 8(a) and (b) depict the standard contour integral I_{-3} for the straightforward and robust formulation, resp. Because approximation (28) has been used in the derivation of the robust formulation, an error in the order of 10^{-2} is present, see Fig. 8(c). This error is much larger that the error in the other expressions of the robust formulation. For illustration purposes, the tolerance regions in these figures have been chosen extremely large. When applied to the MoT scheme, the tolerance regions will be orders of magnitude smaller and the approximation error will drop below machine precision. This has been verified experimentally,

as depicted in Fig. 8(d). For large tolerance values, the approximation error convergences quadratically, as derived in (28). For tolerance values smaller than 10^{-8}, the error remains 10^{-16} because the rounding error dominates the truncation error.

D. Summary of Robust Formulation

The robust formulation that has been derived in Sections V-A–V-C has to be incorporated into the evaluation of the radiation fields. For a given observer point $\tilde{\mathbf{r}}$ and source triangle Γ_q, different expressions for the standard contour integrals (10) have to be used. That is:

- (24) for $\tilde{\mathbf{r}}$ inside edge tolerance regions;
- (25) for $\tilde{\mathbf{r}}$ inside ray tolerance regions;
- (29) for $\tilde{\mathbf{r}}$ inside vertex tolerance regions;
- (15) and (17) for $\tilde{\mathbf{r}}$ outside tolerance regions

where the tolerance regions will be defined in Section VI. All expressions in this robust formulation are well-behaved, because no singular behavior is present and the radiation fields are approximated with a very high accuracy. In fact, all expressions outside the vertex tolerance regions are exact, except of rounding errors. Inside the vertex tolerance regions, an approximation with quadratic convergence w.r.t. the size of the tolerance region has been used.

E. Zero Projection Height

The robust formulation is used when the projection of the observer point is located close to the boundary of the source triangle only. But the derivation is not valid for zero projection height h. This combination of projection on the triangle boundary and a zero projection height can only happen when a quadrature point is located on the triangle boundary. This will never happen for the Gaussian quadrature rules [17]. In fact, the tolerance values are required to be smaller than the distance from each quadrature point to the triangle boundary. This is easily satisfied for most quadrature rules, consequently no additional formulations are necessary for zero projection height.

VI. Tolerance Regions

The tolerance regions are required for finite precision arithmetic, as explained in Section IV. In Section V, accurate expressions for the standard contour integrals have been derived for use within the edge, ray and vertex tolerance regions. In this section, the full definition of the tolerance regions will be established for specific design criteria.

A. Requirements on Tolerance Regions

The tolerance regions will be defined according to the following requirements:

1) the shape is based on parameters u_1, u_2, and v_0 only;
2) regions are disjoint;
3) regions fully cover the triangle boundary; and
4) tolerance values are dimensionless.

$$
\begin{aligned}
&-h\left(I_{-3}^{\mathrm{line},2}+I_{-3}^{\mathrm{line},3}+I_{-3}^{\mathrm{pole}}\right)\\
&\quad=\begin{cases}\arctan\left(\frac{u_{22}}{v_{20}}\frac{h}{|\mathbf{v}_1-\mathbf{r}^\star|}\right)-\arctan\left(\frac{u_{21}}{v_{20}}\frac{h}{|\mathbf{r}_2-\mathbf{r}^\star|}\right)+\arctan\left(\frac{u_{32}}{v_{30}}\frac{h}{|\mathbf{r}_3-\mathbf{r}^\star|}\right)-\arctan\left(\frac{u_{31}}{v_{30}}\frac{h}{|\mathbf{v}_1-\mathbf{r}^\star|}\right)-2\pi, & \text{inside triangle}\\ \arctan\left(\frac{u_{22}}{v_{20}}\frac{h}{|\mathbf{v}_1-\mathbf{r}^\star|}\right)-\arctan\left(\frac{u_{21}}{v_{20}}\frac{h}{|\mathbf{r}_2-\mathbf{r}^\star|}\right)-\pi, & \text{on edge 3}\\ -\alpha_1, & \text{on vertex 1}\end{cases}\\
&\quad\approx\begin{cases}\left(\phi-\alpha_1+\frac{\pi}{2}\right)+\left(\frac{\pi}{2}+\arctan\left(\frac{v_{20}}{u_{21}}\frac{|\mathbf{r}_2-\mathbf{r}^\star|}{h}\right)\right)+\left(\frac{\pi}{2}-\arctan\left(\frac{v_{30}}{u_{32}}\frac{|\mathbf{r}_3-\mathbf{r}^\star|}{h}\right)\right)-\left(\phi-\frac{\pi}{2}\right)-2\pi, & \text{inside triangle}\\ \left(\phi-\alpha_1+\frac{\pi}{2}\right)+\left(\frac{\pi}{2}+\arctan\left(\frac{v_{20}}{u_{21}}\frac{|\mathbf{r}_2-\mathbf{r}^\star|}{h}\right)\right)-\pi, & \text{on edge 3}\\ -\alpha_1, & \text{on vertex 1}\end{cases}\\
&\quad=\arctan\left(\frac{v_{20}}{u_{21}}\frac{|\mathbf{r}_2-\mathbf{r}^\star|}{h}\right)-\arctan\left(\frac{v_{30}}{u_{32}}\frac{|\mathbf{r}_3-\mathbf{r}^\star|}{h}\right)-\alpha_1
\end{aligned}
\tag{29a}
$$

$$
\begin{aligned}
&\frac{2}{h^2}\left(I_0^{\mathrm{line},2}+I_0^{\mathrm{line},3}+I_0^{\mathrm{pole}}\right)\\
&\quad=\begin{cases}v_{20}\frac{|\mathbf{v}_1-\mathbf{r}_2|}{h^2}+\arctan\left(\frac{u_{22}}{v_{20}}\right)-\arctan\left(\frac{u_{21}}{v_{20}}\right)+v_{30}\frac{|\mathbf{r}_3-\mathbf{v}_1|}{h^2}+\arctan\left(\frac{u_{32}}{v_{30}}\right)-\arctan\left(\frac{u_{31}}{v_{30}}\right)-2\pi, & \text{inside triangle}\\ v_{20}\frac{|\mathbf{v}_1-\mathbf{r}_2|}{h^2}+\arctan\left(\frac{u_{22}}{v_{20}}\right)-\arctan\left(\frac{u_{21}}{v_{20}}\right)-\pi, & \text{on edge 3}\\ -\alpha_1, & \text{on vertex 1}\end{cases}\\
&\quad=\begin{cases}v_{20}\frac{|\mathbf{v}_1-\mathbf{r}_2|}{h^2}+\left(\phi-\alpha_1+\frac{\pi}{2}\right)+\left(\frac{\pi}{2}+\arctan\left(\frac{v_{20}}{u_{21}}\right)\right)+v_{30}\frac{|\mathbf{r}_3-\mathbf{v}_1|}{h^2}+\left(\frac{\pi}{2}-\arctan\left(\frac{v_{30}}{u_{32}}\right)\right)-\left(\phi-\frac{\pi}{2}\right)-2\pi, & \text{in triangle}\\ v_{20}\frac{|\mathbf{v}_1-\mathbf{r}_2|}{h^2}+\left(0-\alpha_1+\frac{\pi}{2}\right)+\left(\frac{\pi}{2}+\arctan\left(\frac{v_{20}}{u_{21}}\right)\right)-\pi, & \text{on edge 3}\\ -\alpha_1, & \text{on vertex 1}\end{cases}\\
&\quad=v_{20}\frac{|\mathbf{v}_1-\mathbf{r}_2|}{h^2}+v_{30}\frac{|\mathbf{r}_3-\mathbf{v}_1|}{h^2}+\arctan\left(\frac{v_{20}}{u_{21}}\right)-\arctan\left(\frac{v_{30}}{u_{32}}\right)-\alpha_1
\end{aligned}
\tag{29b}
$$

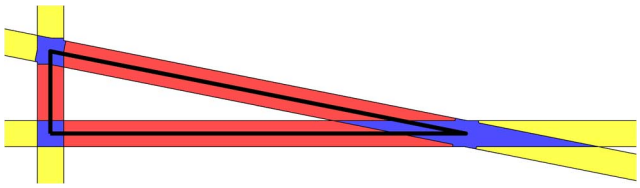

Fig. 9. Tolerance regions with $\epsilon_{\text{edge}} = 0.1$, $\epsilon_{\text{vertex}} = 0.1$ for a triangle given by vertices ([0, 0], [2, 0], [0, 0.4]) and $\sqrt{A} = 0.63$. The vertex tolerance regions are depicted in blue, the edge tolerance regions in red, and the ray tolerance regions in yellow.

The singularities present in the analytical expression of the radiation fields are related to the local parameters u_1, u_2, or v_0, defined by (12). Only these parameter cause singularities at certain locations of the projection point, for which a robust formulation is necessary. Therefore, the tolerance regions will be based on the parameters u_1, u_2, and v_0 only. To this end, two different tolerance values will be used, one for tolerance regions based on u_1 and u_2 and the other for v_0, which will be denoted by ϵ_{vertex} and ϵ_{edge}, resp.

For the exact evaluation of radiation fields, the standard pole integrals have to be evaluated only once for each contour. In the robust formulation, the standard pole integrals are evaluated in each tolerance region. Therefore, the projection point has to be located in only one tolerance region and hence disjoint tolerance regions are required. Because singularities are present on the whole boundary of the source triangle, the tolerance regions should cover the full boundary.

Dimensionless tolerance values will be used because the robust formulation should be applicable to all surface meshes, independent of their length scale and local refinement. To this end, the tolerance values will depend on a characteristic length scale of the source triangle. In this paper, a factor $\sqrt{A_q}$ will be used, where A_q denotes the area of source triangle Γ_q.

B. Definition of Tolerance Regions

The edge, ray, and vertex tolerance regions are denoted by $\mathcal{E}^i_{\text{edge}}$, $\mathcal{E}^i_{\text{ray}}$, and $\mathcal{E}^i_{\text{vertex}}$ for $i = 1, 2, 3$. They are defined by

$$\mathcal{E}^1_{\text{edge}} = \{\tilde{\mathbf{r}} \in \mathbb{R}^3 |\, |v_{10}| < \tilde{\epsilon}_{\text{edge}} \wedge |v_{20}| \geq \tilde{\epsilon}_{\text{edge}} \wedge |v_{30}| \geq \tilde{\epsilon}_{\text{edge}} \wedge u_{11} \geq \tilde{\epsilon}_{\text{vertex}} \wedge -u_{12} \geq \tilde{\epsilon}_{\text{vertex}}\} \tag{30a}$$

$$\mathcal{E}^1_{\text{ray}} = \{\tilde{\mathbf{r}} \in \mathbb{R}^3 |\, |v_{10}| < \tilde{\epsilon}_{\text{edge}} \wedge |v_{20}| \geq \tilde{\epsilon}_{\text{edge}} \wedge |v_{30}| \geq \tilde{\epsilon}_{\text{edge}} \wedge (-u_{11} \geq \tilde{\epsilon}_{\text{vertex}} \vee u_{12} \geq \tilde{\epsilon}_{\text{vertex}})\} \tag{30b}$$

$$\mathcal{E}^1_{\text{vertex}} = \{\tilde{\mathbf{r}} \in \mathbb{R}^3 |\, (|u_{22}| < \tilde{\epsilon}_{\text{vertex}} \wedge |v_{20}| < \tilde{\epsilon}_{\text{edge}}) \vee (|u_{31}| < \tilde{\epsilon}_{\text{vertex}} \wedge |v_{30}| < \tilde{\epsilon}_{\text{edge}}) \vee (|v_{20}| < \tilde{\epsilon}_{\text{edge}} \wedge |v_{30}| < \tilde{\epsilon}_{\text{edge}})\} \tag{30c}$$

and similar for $i = 2, 3$, where $\tilde{\epsilon}_{\text{edge}} = \epsilon_{\text{edge}}\sqrt{A_q}$ and $\tilde{\epsilon}_{\text{vertex}} = \epsilon_{\text{vertex}}\sqrt{A_q}$. Clearly, the tolerance regions are based on the parameters u_1, u_2, and v_0 only and the tolerance values are dimensionless. As can be derived, the tolerance regions are disjoint and cover the full boundary of the triangle. This can be seen in Fig. 9 where the tolerance regions are depicted. Thus, all requirements on the tolerance regions are satisfied.

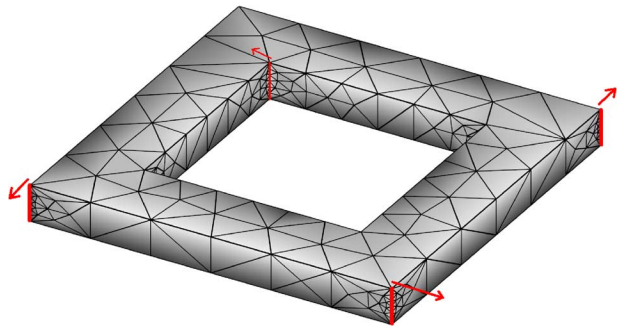

Fig. 10. Surface mesh on the toroidal box of size $1 \times 1 \times 0.1$ m, with the arrows depicting the 10^{-10} m shift of the edges.

A striking feature of this definition is the vertex tolerance region, which is not a circle as one might expect. There are two reasons for the parallelogram shape. First, in order to establish disjoint tolerance regions, the intersection of two edge tolerance regions is considered as a vertex tolerance region. Second, the robust formulation in the edge tolerance regions dictates that the parameters u_1 and u_2 have a strictly positive lower bound. When circles, defined by $\sqrt{(u_1)^2 + (v_0)^2} < \epsilon_{\text{circle}}\sqrt{A_q}$, are used, the parameter u_1 might become arbitrary small when $v_0 \approx \epsilon_{\text{circle}}\sqrt{A_q}$ in edge tolerance regions.

VII. Experimental Confirmation

Two versions for the analytical computation of radiation fields in finite precision arithmetic have been derived in Sections IV and V, namely a straightforward and a robust formulation, resp. The straightforward formulation can be considered as a standard and correct choice to enable finite precision arithmetic and serves its purpose in most cases. The robust formulation on the other hand is more sophisticated and uses well-behaved expressions for the radiation fields. It should be stressed that the two formulations only differ within the tolerance regions. Since tolerance values are very small, hardly any projection points are located inside the tolerance regions for small-scale objects. Therefore, the MoT solutions hardly differ for the two formulations. However, when the TDIE method will be applied for larger geometries, more mesh nodes are required and the likelihood that projection points are located inside the tolerance regions is increased.

Computational methods, like the TDIE method, have to be robust in order to be applied in industry. Through an example we will show that the accuracy of the evaluation of the radiation fields strongly influences the robustness of the algorithm. To this end, a configuration has been generated such that the impact of the tolerance regions is large, but without resorting to uncarefully chosen parameters. This configuration must include many observer points that are projected inside tolerance regions. Then, many radiation fields are computed different for the two exact formulations and differences in the MoT solutions are expected.

The object is given by a toroidal box of size $1 \times 1 \times 0.1$ m, modeled with a surface mesh of 628 triangular facets, locally refined near the vertical edges of the box. As depicted in Fig. 10, all vertical edges of the box are artificially shifted 10^{-10} m to create a challenging test case. Notice that this shift of mesh

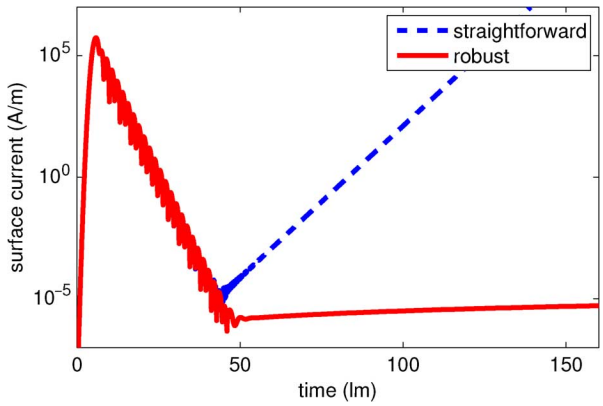

Fig. 11. Magnitude of the electric surface current density at the point (0.967, 0.749, 0.1) on the toroidal box, with two different formulations for analytical expressions of the radiation fields.

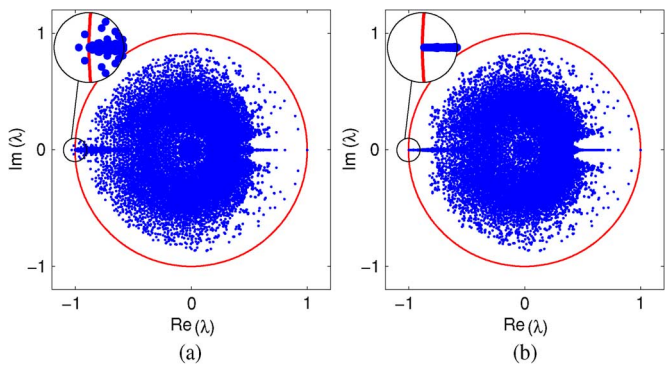

Fig. 12. Eigenvalues (blue markers) of the MoT scheme on the toroidal box and the unit circle (red line) in the complex plane. The zoom box depicts the eigenvalues that determine stability. (a) Straightforward formulation. (b) Robust formulation.

nodes is within the accuracy of almost all mesh generating programs. Because of the shift of the vertical edges of the box, all observer points on the adjacent face of the box are projected inside tolerance regions. The tolerance values are set as $\epsilon_{\text{edge}} = 10^{-8}$ and $\epsilon_{\text{vertex}} = 10^{-8}$.

The EFIE (1) has been discretized with RWG test and basis functions in space and quadratic spline basis functions in time [14]. The outer integral over observer elements is evaluated with a 7-point Gaussian quadrature. The incident field is given by a Gaussian plane wave, defined as

$$\mathbf{E}^i(\mathbf{r},t) = \frac{4}{\sqrt{\pi}T} e^{-\left(\frac{4(c(t-t_0)-\mathbf{r}\cdot\mathbf{k})}{T}\right)^2} \mathbf{p} \tag{31}$$

with polarization $\mathbf{p} = \hat{\mathbf{x}}$, propagation $\mathbf{k} = -\hat{\mathbf{z}}$, width $T = 4$ m, and offset $t_0 = 6$ lm. No accelerator, such as the PWTD [1] and TD-AIM [2], has been used.

The magnitude of the electric surface current density is depicted in Fig. 11 for 1600 timesteps. Initially, no differences are visible between the two formulations. At late-time, however, the straightforward formulation with constant approximation results in a surface current that grows beyond any bound. The novel robust formulation on the other hand remains stable. This difference in stability has also been verified with a spectral analysis, depicted in Fig. 12. The MoT scheme is stable if the spectral radius ρ of the amplification matrix is smaller than one [11]. For this test case, $\rho = 1.029$ and $\rho = 1.0$ for the straightforward and robust formulation, resp.

VIII. Conclusion

The quasi-exact integration method is a key to the successful application of MoT schemes in TDIE methods for electromagnetics. Available analytical expressions for the exact evaluation of the radiation fields have to be reformulated for evaluation in finite precision arithmetic. The straightforward formulation does not necessarily lead to the accuracy required for late-time stability of the MoT scheme, because it is not well-behaved for a number of limit cases. This is confirmed with a computational experiment. Hence, a novel formulation with well-behaved expressions has been derived in this paper, along with specifically designed tolerance regions. This robust formulation does not impinge on the overall accuracy of the quasi-exact integration method and results in a stable MoT scheme.

References

[1] B. Shanker, A. A. Ergin, K. Aygün, and E. Michielssen, "Analysis of transient electromagnetic scattering phenomena using a two-level plane wave time-domain algorithm," *IEEE Trans. Antennas Propag.*, vol. 48, no. 4, pp. 510–523, Apr. 2000.

[2] A. E. Yılmaz, J.-M. Jin, E. Michielssen, and D. S. Weile, "A fast Fourier transform accelerated marching-on-in-time algorithm for electromagnetic analysis," *Electromagn.*, vol. 21, pp. 181–197, 2011.

[3] H. Bağci, A. E. Yılmaz, J.-M. Jin, and E. Michielssen, "Fast and rigorous analysis of EMC/EMI phenomena on electrically large and complex cable-loaded structures," *IEEE Trans. Electromagn. Compat.*, vol. 49, no. 2, pp. 361–381, Feb. 2007.

[4] E. van 't Wout, H. van der Ven, D. R. van der Heul, and C. Vuik, "A provably stable MoT scheme based on quadratic spline basis functions," presented at the IEEE Int. Symp. Antennas Propagation, Chicago, IL, USA, 2012.

[5] A. Sadigh and E. Arvas, "Treating the instabilities in marching-on-in-time method from a different perspective," *IEEE Trans. Antennas Propag.*, vol. 41, no. 12, pp. 1695–1702, Dec. 1993.

[6] S. J. Dodson, S. P. Walker, and M. J. Bluck, "Implicitness and stability of time domain integral equation scattering analyses," *ACES J.*, vol. 13, pp. 291–301, 1998.

[7] T. Abboud, J.-C. Nédélec, and J. Volakis, "Stable solution of the retarded potential equations," in *Proc. ACES Conf.*, Monterey, CA, USA, 2001, pp. 146–151.

[8] D. S. Weile, G. Pisharody, N.-W. Chen, B. Shanker, and E. Michielssen, "A novel scheme for the solution of the time-domain integral equations of electromagnetics," *IEEE Trans. Antennas Propag.*, vol. 52, no. 1, pp. 283–295, Jan. 2004.

[9] X. Wang, R. A. Wildman, D. S. Weile, and P. Monk, "A finite difference delay modeling approach to the discretization of the time domain integral equations of electromagnetics," *IEEE Trans. Antennas Propag.*, vol. 56, no. 8, pp. 2442–2452, Aug. 2008.

[10] B. Shanker, M. Lu, J. Yuan, and E. Michielssen, "Time domain integral equation analysis of scattering from composite bodies via exact evaluation of radiation fields," *IEEE Trans. Antennas Propag.*, vol. 57, no. 5, pp. 1506–1520, May 2009.

[11] F. P. Andriulli, K. Cools, F. Olyslager, and E. Michielssen, "Time domain Calderón identities and their application to the integral equation analysis of scattering by PEC objects part II: Stability," *IEEE Trans. Antennas Propag.*, vol. 57, no. 8, pp. 2365–2375, Aug. 2009.

[12] Y. Shi, M.-Y. Xia, R.-S. Chen, E. Michielssen, and M. Lu, "Stable electric field TDIE solvers via quasi-exact evaluation of MoT matrix elements," *IEEE Trans. Antennas Propag.*, vol. 59, no. 2, pp. 574–585, Feb. 2011.

[13] A. J. Pray, N. V. Nair, and B. Shanker, "Stability properties of the time domain electric field integral equation using a separable approximation for the convolution with the retarded potential," *IEEE Trans. Antennas Propag.*, vol. 60, no. 8, pp. 3772–3781, Aug. 2012.

[14] E. van 't Wout, D. R. van der Heul, H. van der Ven, and C. Vuik, "Design of temporal basis functions for time domain integral equation methods with predefined accuracy and smoothness," *IEEE Trans. Antennas Propag.*, vol. 61, no. 1, pp. 271–280, Jan. 2013.

[15] S. M. Rao, D. R. Wilton, and A. W. Glisson, "Electromagnetic scattering by surfaces of arbitrary shape," *IEEE Trans. Antennas Propag.*, vol. AP-30, no. 3, pp. 409–418, Mar. 1982.

[16] G. Manara, A. Monorchio, and R. Reggiannini, "A space-time discretization criterion for a stable time-marching solution of the electric field integral equation," *IEEE Trans. Antennas Propag.*, vol. 45, no. 3, pp. 527–532, Mar. 1997.
[17] D. A. Dunavant, "High degree efficient symmetrical Gaussian quadrature rules for the triangle," *Int. J. Numer. Meth. Eng.*, vol. 21, pp. 1129–1148, 1985.

Elwin van 't Wout was born in Rotterdam, The Netherlands, in 1986. He received the M.S. degree in applied mathematics from the Delft University of Technology, Delft, The Netherlands, in 2009. The research for his Master's thesis was carried out at the Maritime Research Institute, The Netherlands. He is prusuing the Ph.D. degree under the supervision of Prof. C. Vuik at the Delft University of Technology.

In 2009, he joined the National Aerospace Laboratory NLR, Amsterdam, The Netherlands. His research focuses on time domain integral equation methods.

Duncan R. van der Heul was born in Rotterdam, The Netherlands, in 1973. He received the M.S. degree in marine technology from the Delft University of Technology, Delft, The Netherlands, in 1997, and the Ph.D. degree in applied mathematics in 2002 under the supervision of Prof. Wesseling.

From 2001 to 2008, he was a Research Engineer at the National Aerospace Laboratory NLR, Amsterdam, The Netherlands. In 2008, he joined the Numerical Analysis Group of Prof. Vuik at the Delft University of Technology as an Assistant Professor, where he focuses his research on computational fluid dynamics and computational electromagnetics.

Harmen van der Ven received the M.S. degree in mathematics and the Ph.D. degree from Utrecht University, Utrecht, The Netherlands, in 1989 and 1993, respectively.

Thereafter, he joined the Netherlands National Aerospace Laboratory, Amsterdam, The Netherlands, where he now holds the position of Senior Scientist. His research interest is computational science with applications in electromagnetics, fluid dynamics, and mechanical engineering. In the field of electromagnetics, the main focus is on the prediction of radar cross sections of large objects with radar absorbing treatment.

Cornelis Vuik received the M.S. degree in applied mathematics from the Delft University of Technology, Delft, The Netherlands, in 1982. After a short stay at the Philips Research Laboratories, he received the Ph.D. degree in mathematics from Utrecht University, Utrecht, The Netherlands, in 1988.

Thereafter, he joined the Delft University of Technology, where he holds the position of Full Professor in the Numerical Analysis Research Group. In 2007, he also became Director of the Delft Center of Computational Science and Engineering, and in 2012, the Scientific Director of the 3TU Applied Mathematics Institute.